HHS Public Access

Author manuscript

Biofabrication. Author manuscript; available in PMC 2019 May 02.

Published in final edited form as:

Biofabrication. ; 10(3): 035007. doi:10.1088/1758-5090/aabe0b.

Photolithographic-Stereolithographic-Tandem Fabrication of 4D Smart Scaffolds for Improved Stem Cell Cardiomyogenic Differentiation

Shida Miao[1], **Haitao Cui**[1], **Margaret Nowicki**[1], **Se-jun Lee**[1], **José Almeida**[1], **Xuan Zhou**[1], **Wei Zhu**[1], **Xiaoliang Yao**[1], **Fahed Masood**[2], **Michael W. Plesniak**[1,4], **Muhammad Mohiuddin**[3], and **Lijie Grace Zhang**[1,4,5]

[1]Department of Mechanical and Aerospace Engineering, The George Washington University, Washington DC 20052, USA

[2]Department of Mechanical Engineering, University of Maryland, College Park, MD 20742, USA

[3]Program in Cardiac Xenotransplantation, Department of Surgery, University of Maryland, Baltimore, MD 21201, USA

[4]Department of Biomedical Engineering, The George Washington University, Washington DC 20052, USA

[5]Department of Medicine, The George Washington University, Washington DC 20052, USA

Abstract

4D printing is a highly innovative additive manufacturing process for fabricate smart structures with the ability to transform over time. Significantly different from regular 4D printing techniques, this study focuses on creating novel 4D hierarchical micropatterns using a unique photolithographic-stereolithographic-tandem strategy (PSTS) with smart soybean oil epoxidized acrylate (SOEA) inks for effectively regulating human bone marrow mesenchymal stem cell (hMSC) cardiomyogenic behaviors. The 4D effect refers to autonomous conversion of the surficial-patterned scaffold into a pre-designed construct through an external stimulus delivered immediately after printing. Our results show that hMSCs actively grew and were highly aligned along the micropatterns, forming an uninterrupted cellular sheet. The generation of complex patterns was evident by triangular and circular outlines appearing in the scaffolds. This simple, yet efficient, technique was validated by rapid printing of scaffolds with well-defined and consistent micro-surface features. A 4D dynamic shape change transforming a 2-D design into flower-like structures was observed. The printed scaffolds possessed a shape memory effect beyond the 4D features. The advanced 4D dynamic feature may provide seamless integration with damaged tissues or organs, and a proof of concept 4D patch for cardiac regeneration was demonstrated for the first time. The 4D fabricated cardiac patch showed significant cardiomyogenesis confirmed by immunofluorescence staining and qRT-PCR analysis, indicating its promising potential in future tissue and organ regeneration applications.

Corresponding author: Dr. Lijie Grace Zhang, Tel: 202-994-2479, Fax: 202-994-0238, lgzhang@gwu.edu, Mailing Address: 800 22nd Street NW Science and Engineering Hall, Room 3590, Washington DC, 20052.

Graphical Abstract

This study focused on creating 4D hierarchical micropatterns using a unique photolithographic-stereolithographic-tandem strategy (PSTS) for effectively regulating human bone marrow mesenchymal stem cell (hMSC) cardiomyogenic behaviors. Unique surface micro-patterns are 4D printed with soybean oil epoxidized acrylate (SOEA) in an innovative manner. A thin ink film (10 μm depth) is observed after photolithography and is further used to generate micro-patterns. The 4D effect refers to the autonomous conversion of the micro-patterned flat sheet into a pre-designed construct by external stimulus. Moreover, the scaffold possesses shape memory properties beyond the 4D feature. Cardiomyogenesis of hMSCs on the fabricated scaffolds is confirmed by immunofluorescence staining and qRT-PCR analysis, indicating great application potential for future tissue and organ regeneration applications.

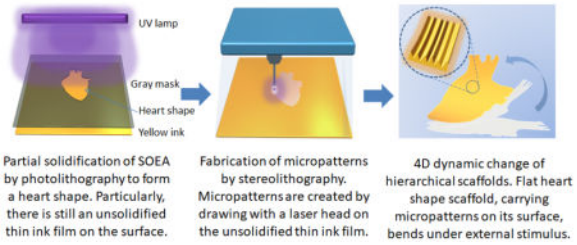

Keywords

4D printing; photolithography; stereolithography; cardiac patch; tissue engineering; organ regeneration

1. Introduction

There is an urgent need for developing improved tissue and organ substitutes to replace traditional treatment methods that fail to meet patients' needs. For example, an average of 22 people die each day due to scarcity of donor tissues or organs in the United States [1]. Tissue engineering aims to fabricate biomedical scaffolds with multiple functions and may provide viable solutions for these challenges [2–4]. 3D printing has garnered great attention for transforming the tissue engineering field. 3D printing has advantages in constructing complicated structures, customizing mass distribution, and minimizing weight/volume while achieving requisite strength and other properties. This is especially relevant for patient-specific manufacturing. Beyond 3D printing, 4D printing refers to 3D printing of objects which can, immediately after printing, self-transform in form or function when exposed to a predetermined stimulus[5–10]. The various applied stimuli include osmotic pressure, heat, current, ultraviolet light, or other energy sources [5–10]. Although 4D printing technology is still in its infancy, the advanced 4D self-assembly feature is extremely promising for tissue engineering in that this dynamic processes may achieve minimally invasive surgical delivery, seamless integration, and mimic the dynamically changing morphologies of native tissues and organs [10].

In addition to external architecture, a crucial feature of natural tissues and organs is highly organized and structurally anisotropic components. Creating biomimetic topographical cues

on tissue engineered scaffolds to recapitulate native cellular microenvironments has a tremendous impact on improving tissue and organ regeneration. Just take aligned surface topography as an example, when multi-lineage differentiation of mesenchymal stem cells and progenitor cells was conducted on aligned collagen matrices, the aligned pattern not only influenced myotube assembly and enhanced myotube organization and length, but also resulted in ordered matrix mineralization during osteogenesis of human bone marrow mesenchymal stem cells (hMSCs) [11]. In addition, during neonatal rat mesenchymal stem cell cardiomyogenic differentiation, the time course and degree of functional integration with surrounding cardiac tissue was greatly affected by forced cell alignment [12].

Considering the significantly favorable feature of topographical cues, various manufacturing methods have been employed to develop specific nano/micro structures for regulating cell behaviors. For instance, electrospinning has been a widely applied process for producing aligned nanofibers to induce the organization of cellular sheets [13–16]. Anisotropic nano architectures, assembled by magnetic-field-directed self-assembly, provided sufficient physical cues to align cells independent of the extracellular matrix composition [17]. Microgrooves generated by uniaxially stretching poly (ε-caprolactone) films provided geometric cues to align hMSCs [18–20]. Photolithographic techniques have been notably utilized to pattern microchannels for aligning stem cells by applying polydimethylsiloxane (PDMS) as a constructing material [21, 22]. Although these studies greatly advanced this research field, it is still challenging to fabricate biomimetic tissue scaffolds in the manner of integrating the topographical cues into a hierarchical architecture. Thus, we expect a multi-scale fabricating technique, featuring a simple and versatile approach for generating topographical surface structures on a macro-architecture, may significantly advance related studies in the future [23, 24].

Herein, we used smart natural lipids (i.e., soybean oil epoxidized acrylate (SOEA)) as ink material to fabricate biocompatible, topographical, and 4D dynamic shape-changing tissue scaffolds. SOEA is derived from soybean oil which is a natural, renewable resource and is attracting greater attention as biomaterials in recent years [25, 26]. We expect that SOEA could provide new features for scaffold fabrication since it is fairly new as an ink material used in 3D/4D printing. We developed unique surface micropatterns with SOEA in an innovative manner. This strategy provided stable surface structures over a large area, favorable biocompatibility, and optimal integration for effectively regulating behavior of hMSCs. Photolithographic-stereolithographic-tandem strategy (PSTS), referring to the sequential treatment of the same ink feedstock with photolithography and stereolithography (Figure 1), was utilized, where a 10 μm depth liquid film was observed for the first time after photolighography and further solidified with stereolithography to generate complex micro-patterns. Compared to previously reported works, this study illustrated that scaffolds fabricated with a PSTS process not only possess subtle surface micropatterns but also exhibit dynamic 4D shape change after external stimulation. The 4D smart shape change property may provide seamless integration with damaged tissues or organs [10]. Considering the PSTS scaffolds are film-like structures, the PSTS technique has great potential for development of patching scaffolds. Stem cell cardiomyogenesis on the PSTS cardiac patch was tested by immunofluorescence staining and qRT-PCR analysis. Greater marker

expression on 4D scaffolds was observed, indicating the application potential in cardiac patches.

2. Materials and methods

2.1 Reagents and materials

Soybean oil epoxidized acrylate (SOEA, contains 4,000 ppm monomethyl ether hydroquinone as inhibitor), formaldehyde 10% (neutral buffered), and acetone (≥99.5%) were obtained from Sigma-Aldrich (MO, USA). Bis (2,4,6-trimethylbenzoyl)-phenylphosphineoxide (Ciba Irgacure 819) was purchased from Ciba Specialty Chemicals (Basel, Switzerland). Alpha minimum essential medium (MEM Alpha (1×)+Gluta MAX™-1), Texas Red®-X Phalloidin, l-glutamine and penicillin/streptomycin solution were obtained from Thermo Fisher Scientific (MA, USA). Fetal Bovine Serum (FBS) was purchased from Gemini Bioproducts (CA, USA). DAPI (4″,6 - Diamidino - 2 - phenylindole, dihydrochloride) was purchased from Anaspec Inc (CA, USA). Phosphate-buffered saline (PBS), without calcium & magnesium, and Trypsin/EDTA (1× 0.25% Trypsin/2.21 mM ethylenediaminetetraacetic acid (EDTA) in Hank's balanced salt solution without sodium bicarbonate, calcium and magnesium) were supplied by Mediatech Inc (VA, USA). Primary hMSCs were obtained from healthy consenting donors at the Texas A&M Health Science Center, Institute for Regenerative Medicine.

2.2 Preparation of 4D printing ink

100 g SOEA was mixed with 100 mL acetone in a 500 mL brown glass bottle wrapped with two layers of aluminum foil to protect the mixture from light. Then, 1.26 g bis(2,4,6-trimethylbenzoyl)-phenylphosphineoxide was added. The mixture was shaken mildly by hand and a 150 rpm Standard Analog Shaker (VWR International, PA, USA) alternatively to reach a homogenous yellow solution that was subsequently put into a container under vacuum overnight to remove the acetone. The final product was a sticky yellow liquid and used directly as smart ink for 4D printing.

2.3 Design of scaffolds

The expected structure was drawn with Autodesk123D software (Autodesk Inc, CA, USA), and saved as a .stl format file which was then loaded into the software Slic3r which is licensed under the GNU Affero General Public License, version 3. The infill density and the printing speed were assigned in Slic3r. Other typical parameters assigned in Slic3r include: 0.2 mm layer height, 0.2 mm first layer height; vertical shells - perimeters 0; horizontal shells – solid layers, top 0, bottom 0; 90 ° infill angle, 10 mm^2 solid infill threshold area; skirt, loop 0; extrusion width, first layer 0%.

2.4 4D printing protocol

A typical PSTS printing of SOEA, where photolithographic and stereolithographic strategies were used in tandem, is illustrated in Figure 1. First, we developed the complex outline of the desired biomedical scaffolds by applying the method of soft lithography which is widely applied for lab-on-a-chip applications [27]. Compared to a complicated master device used in soft lithography studies, we easily printed shadow masks of the scaffold's outline with

acrylonitrile butadiene styrene (Fortus 250mc, Stratasys, MN). A predesigned structure was photolithographically obtained with desired complex outlines such as triangles and circles. A thin liquid film (10 μm depth) was observed after photolithography, which, to the best of our knowledge, has never been reported previously and will be further discussed in "Results and discussion". We assume this particular phenomenon is a crucial feature for new topographic generation. Second, the unsolidified thin liquid film was subsequently printed as ink via a table top stereolithography system developed in our lab based on the existing Solidoodle® 3D printer platform [28]. A typical stereolithography set-up consists of a container with a liquid photopolymerizable resin and a UV laser held by galvanometers [29]. Directed by a CAD program, the laser beam traces a design onto the resin creating a hardened layer. Here, we replaced the ink container with the unsolidified thin liquid film, and the unpolymerized thin liquid layer is thereafter selectively solidified by the high intensity laser beam. After PSTS printing, the fabricated scaffold was soaked overnight in 95% ethanol to remove unpolymerized ink and photo initiator. Lastly, the scaffold was sterilized with 70% ethanol for 30 min and soaked in phosphate buffered saline (PBS) overnight prior to cell culturing.

2.5 Cell culture and adhesion study

hMSCs (passage No. 3–6) were cultured in complete media composed of alpha minimum essential medium supplemented with 16.5% fetal bovine serum (FBS), 1% (v/v) l-glutamine, and 1% penicillin:streptomycin solution, under standard cell culture conditions (37 °C, a humidified, 5% CO_2/95% air environment). For hMSC attachment studies, the 4D test samples were cut into 8 mm diameter specimens. hMSCs were seeded at a cell density of 50,000 cells/specimen, and cultured for 4 hours. The specimens were washed three times with PBS to remove non-adherent cells. The attached cells were lifted with trypsin/EDTA, quantified with a CellTiter 96″ Aqueous Non-Radioactive Cell Proliferation Assay, and analyzed spectrophotometrically using a Thermo Scientific Multiskan GO Spectrophotometer at 490 nm.

2.6 Cell alignment analysis

For cell alignment observation, hMSCs were seeded at a cell density of 100,000 cells/specimen (8 mm diameter), and cultured under standard cell culture conditions for 3 days. Media was exchanged every other day. The specimens were washed three times with PBS to remove non-adherent and dead cells. The cells were subsequently fixed with 5% formalin and permeabilized in 0.1% Triton X-100. After rinsing with PBS, the remaining cells were stained with Texas red fluorescent dye (to stain the cells' cytoskeleton) for 30 minutes and then DAPI blue fluorescent dye (to stain the cells' nuclei) for 15 min. The double-stained samples were imaged on a Zeiss LSM 710 confocal microscope.

The alignment of hMSCs was quantified using reported methods with a slight modification [11]. The confocal images were analyzed with NIH Image J software 1.49 V (National Institutes of Health, USA). The cells were isolated from the background by setting a threshold value of the reflection intensity. The direction of the microchannels, or microgrooves, was set as an angle of 0°. The cell major axis with respect to the direction of

the microchannels or microgrooves was defined as the cell orientation. Cells were considered to be aligned if their angles fell into ± 10° from the original benchmark.

2.7 Cardiomyogenic differentiation and immunofluorescence analysis

hMSCs were seeded at a cell density of 200,000 cells/specimen, and cultured in complete media under standard cell culture conditions for 24 hours. Then cardiomyogenic differentiation media (complete media plus 5-azacytidine, a chemical induction agent) was added, and cultured for 24 hours. After that, the samples were cultured in the complete media for 3 weeks, and the media was exchanged every other day.

At a predesigned time, the samples were fixed with 10% formalin for 15 minutes, permeabilized in 0.1% Triton X-100 for 10 minutes and blocked in 5% bovine serum albumin solution for 30 minutes. Then cells were incubated with primary antibodies at 4°C overnight. The following primary antibodies for detecting cardiomyogenesis were used to stain: mouse monoclonal anti-Cardiac Troponin I antibody (Santa Cruz Biotechnology) and rabbit polyclonal anti-Sarcometic Alpha Actinin antibody (Abcam). Troponin I (cTnI) is cardiac regulatory proteins that control the calcium mediated interaction between actin and myosin. Sarcometic Alpha Actinin is a specific alpha-cardiac actinin, existing as Z lines and dots in stress fibers of myotubes in cardiac muscle. After incubation with primary antibodies, goat anti-mouse IgG-H&L (Alexa Fluor® 594) (Abcam) and goat anti-rabbit IgG-H&L (Alexa Fluor® 488) (Abcam) were added as secondary antibodies and incubated for 1 hour, respectively. Finally, the nuclei were stained with DAPI. Fluorescence images were observed, and captured using a confocal microscope.

2.8 Quantitative RT-PCR

The cardiomyogenic gene expression of all samples including myosin heavy chain (MHC), desmin, and myocardin (MyoC) were analyzed by real-time quantitative reverse transcription polymerase chain reaction (qRT-PCR) assay. The RNA purification was performed per the protocol provided by Life Technologies Company. Specifically, the total RNA contents were extracted from the samples by using Trizol reagent. The RNA quality and concentration were determined from the absorbance at 260 and 280 nm with a microplate reader. RNA samples were reverse-transcribed to cDNA using a Prime Script™ RT reagent Kit (TaKaRa). RT-PCR was then performed on a CFX384 Real-Time System (BIORAD) by using SYBR Premix Ex Taq™ (TaKaRa) according to the manufacturer's protocol. The gene expression level of target genes was normalized against the house keeping gene glyceraldehyde 3-phosphate dehydrogenase (GAPDH). The relative gene expression of the 4D printed scaffold was normalized against the control group to obtain relative gene expression fold values, and calculated via the 2-delta delta ($2^{-\Delta\Delta}$Ct) cycle-threshold method. Primer sequences are as follows: GAPDH, forward primer 5′-ATGTTCGTCATGGGTGTGAA-3′ and reverse primer 5′-TGTGGTCATGAGTCCTTCCA-3′; MHC, forward primer 5′-GATGGCACAGAAGTTGCTGA-3′ and reverse primer 5′-CTTCTCGTAGACGGCTTTGG-3′; desmin, forward primer 5′-TCGGCTCTAAGGGCTCCTC-3′ and reverse primer 5′-CGTGGTCAGAAACTCCTGGTT-3′; MyoC, forward primer 5′-

CTCGGCTTCCTTTGAACAAG-3′ and reverse primer 5′-CTTCCCAGAGAATCCATCCA-3′.

2.10 Statistical analysis

Statistics for quantitative tests were performed using ANOVA and Tukey's multiple pairwise comparison ($p < 0.05$ for significance) unless otherwise stated. Values reported are mean ± standard deviation, n=6, and significant differences are specified in figures.

3. Results and discussion

3.1 The unique unsolidified thin liquid film

During PSTS printing, an unsolidified thin liquid film was observed after photolithography. Accordingly, this phenomenon was further investigated through a curing-drawing experiment, as shown in Figure 2(a). Solidification of SOEA was observed as expected, but a very thin, sticky, unpolymerized SOEA layer on the top of solidified SOEA was confirmed; softly drawing on the unsolidified thin film on the surface of the polymerized SOEA creates the drawn pattern noticeable in Figure 2(b). How this mechanism was created is not completely understood, and it is assumed that complete polymerization is hindered by the relatively higher oxygen concentration at the air/oil interface. In consideration of the molecular structure of SOEA, which is obtained by reacting acrylate acid with epoxidized soybean oil, we compared SOEA to acrylate acid (AA), methyl acrylate acid (MAA), methacrylate acid (MA) and methyl methacrylate acid (MMA). Polymerized AA and MA are white and brittle while polymerized MAA and MMA are transparent, similar with polymerized SOEA (Figure 2(c)). However, the unpolymerized thin liquid film was not detected for those materials, indicating that this property is unique to SOEA. Additionally, SOEA is easily operable and suitable as an ink material in view of its non-volatile property while other chemicals have strong odors and volatilize rapidly in the air.

3.2 The uneven distribution of laser beam

The laser beam is critical for ink solidification during stereolithography as shown in Figure 3. The distance from the laser head to the ink surface is 2 mm and a bright light dot is clearly visible as a dark board is placed under the laser head (Figure 3(a)). As the distance between the laser and the dark board is increased, we observed that the beam spreads out with non-uniform intensity, especially as the distance approaches 4 cm (Figure 3(b–d)). This non-uniform intensity is further confirmed by converting the light spot into black/white, manipulating with an intensity threshold value in a range from 0 (black) to 255 (white) (Figure 3(e)). When the threshold value is 80, a white scattered light spot is clearly visible; distribution of higher energy spots is readily available by increasing the threshold value, as shown in Figure 3(e)-iii with threshold value 110. The non-uniform laser beam intensity distribution might be an unfavorable property in laser beam studies, but this unique feature is important here and will be used for the first time to develop aligned microgrooves.

3.3 Surface microstructures of fabricated scaffolds

Through stereolithography, SOEA can be directly polymerized in a classical process. Samples fabricated by stereolithography are compared with the samples created with the

PSTS technique in the present study. Through stereolithography of SOEA, microgrooves were generated on the bottom surfaces of control samples while their top surfaces are flat. The aligned microstructures are displayed in Figure 4(a); by adjusting the infill density (represented in percentages indicating how much the resulting solid model is filled in with material according to Slic3r software; here the distance between printed lines is controlled by adjusting the infill density), a series of micropatterns with varying groove sizes are readily obtained. The groove-forming mechanism is assumed to be the result of the cone-shaped laser beam. When the laser passes over SOEA, the profile of the solidified SOEA will be close to a triangle. As the infill density is 60%, the printed microstructure is exactly the estimated triangle as seen in Figure 4(a)-i. When the infill density is higher than 60%, the triangles will overlap each other, forming the aligned wrinkle-like microstructures as shown in Figures 4(a) ii–v.

In contrast, PSTS fabricated microstructures are remarkably different (Figure 4(b)). The non-stereolithographic area forms microchannels, while the laser-illuminated area forms ridges (Figure 4(b)-i). By adjusting the infill density, a series of micropatterns with different channel widths can be readily obtained. Moreover, additional microgrooves were generated on the ridges of these scaffolds, which are caused by the uneven distribution of the laser light (Figure 4(b)-iv). The fractured profile of the ridge indicates that its thickness is approximately 10 μm (Figure 4(b)-v). Although both stereolithographic samples and PSTS samples possess aligned microstructures, the width of grooves on stereolithographic samples reaches 400 μm (Figure 4(a)-i) and exhibits random wrinkle distribution (Figures 4(a) ii–v); the depth of their grooves is a wide range of 30–260 μm (Figure 4(a)-vi). The PSTS samples have an adjustable channel width and their channel depth is about 10 μm, while the depth of the microgrooves on the ridges is only 3 μm (Figure 4(b)-vi). The micro-surficial structure on the ridges of the PSTS samples is also observable with a microscope, which further confirms the highly aligned topographical cues generated by stereolithography (Figure 4(c)). The fine microstructures on the samples developed by the PSTS technique may better mimic topographic native tissue microenvironments.

3.4 hMSC behavior on fabricated scaffolds

All fabricated scaffolds were investigated for hMSCs alignment, and the results are shown in Figure 5. On the stereolithographic samples, the cells attach inside the grooves, spread and expand, aligning with the groove direction, which is assumed to be the major mechanism for cell alignment on the micropatterns (Figure 5(a)). From the side view, hMSCs not only fall into the grooves but also spread on the steep sidewalls on either side of the grooves (Figures 5(a) a2–c2); this may be due to the rough surfaces of the sidewalls, which support cell attachment. When the infill is higher than 60%, the micropatterns are wrinkle-like, and the cell sheet becomes flatter as the infill value increases (Figures 5(a) d1–i1, d2–i2). For the PSTS samples, the channels partially share the same characteristics with channels fabricated using photolithographic techniques; that is, micropatterns fabricated using both techniques have flat bottoms. The width of the channel also has a great effect on the cell alignment (Figures 5(b) j1–r1, j2–r2). When the infill is 30%, the channel width is about 250 μm and the hMSCs do not grow solely along the direction of the channel. When the infill is 50%, the channel width is 120 μm and the alignment of hMSCs is noticeable. Moreover, when the

infill is 70%, the channel width is 65 μm, which is closer to the length of a normal hMSC, and the cells are highly aligned in the direction of the channel. When the hMSCs are growing inside the channels with widths approaching the cell length, they may sense the walls of channels and adjust their direction of growth. Additionally, hMSCs spread on the microgrooves of the ridges (Figures 5(b), o2, r2). The growth of hMSCs on the ridges may be due to the low channel depths (approximately 10 μm). The well-aligned microgrooves, averaging roughly 3 μm in width, on the ridges may have been another contributing factor. The microgrooves provide structures similar in size to the structures formed by stretching polycaprolactone (PCL) films, indicating this scale of topographical cues may be favorable for hMSC adhesion and growth [18–20]. Compared to stretched PCL film, the microgrooves created by the PSTS have a longer linear range, which is a potential benefit for cell alignment. The hMSCs growing on both channels and ridges are closely connected and form one continuous cellular sheet (Figures 5(b), o2, r2). Although both stereolithographic and PSTS samples can align hMSCs, it is very clear that the PSTS samples exhibit a smooth and well-organized cell sheet while the stereolithographic samples show rough and un-evenly distributed cells. Therefore, only PSTS samples were used for cardiomyogenic differentiation studies in later sections.

The alignment of hMSCs on the printed scaffold was quantified and the results are depicted in Figure 6(a), further confirming that all micropatterns can direct the alignment of hMSCs. Among the fabricated micropatterns, the PSTS sample with an infill of 70% shows the highest alignment efficiency. The highly aligned microgrooves on the ridges may lead to this efficient alignment. In comparison to a sample with a 50% infill, the narrower channel width on the 70% sample was credited with the improved alignment. In contrast, the uneven surfaces and wrinkle-like structures of the micropatterns on the stereolithographic samples may be responsible for their relatively lower alignment compared to the PSTS sample at an infill of 70%.

3.5 Cytocompatibility of SOEA based scaffolds

In reported works regarding cell alignment, the most often applied polymeric materials are PDMS and PCL, both supporting the attachment and growth of hMSCs [18, 30]. The polymerized SOEA was compared to PDMS and PCL regarding their biocompatibility for hMSC proliferation. As shown in Figure 6(b), over all time points, both PCL and the polymerized SOEA showed significantly higher cell number than PDMS which is widely utilized for studying cell alignment with photolithography techniques. No statistical difference is found between the polymerized SOEA and PCL. Considering the favorable cell biocompatibility of the polymerized SOEA, together with the processing features of the PSTS technique, SOEA has great application potential for cell-aligned tissue engineering.

3.6 Fabrication of scaffolds with complex patterns

The self-established stereolithography and PSTS techniques are not only suitable for linear micropatterns but also easily replicate other complicated patterns such as a triangle (Figure 7(a)) and a circle (Figure 7(b)). As shown in Figure 7(a) a–d, a triangle scaffold was developed by stereolithography of SOEA, and the hMSCs grew along the pattern. As shown in Figures 7(b) a–d, a circular scaffold was fabricated by the PSTS, and the hMSCs

proliferated along the designed direction. The hMSCs not only grew in the channels but also on ridges, forming a particularly uninterrupted circular cell sheet. Compared to the stereolithography, a uniform and well-organized cell sheet was obtained through PSTS, as mentioned earlier. These demonstrations suggested that the PSTS procedure developed in this study is versatile, creating various cell alignment patterns. Additionally, this PSTS technique is simple, fast and easy for fabrication of complex, large scaffolds. As demonstrated in Figure 7(c), a scaffold is developed from the logo of The George Washington University. The outline of the logo was first drawn in the 123D software; the aligned pattern established in the Sli3r software is shown in Figure 7(c)–b. The desired structure was then obtained with the printing system. In order to observe the whole structure, the scaffold was scanned with a scanner (Xerox D95 Copier-Printer from Xerox, Norwalk, CT). The scanned image is shown in Figure 7(c)–c but nothing is observable with the naked eye because the polymerized SOEA is transparent and very light in color. By increasing the light contrast of this image in Photoshop software (Adobe Photoshop CC2014, San Jose, CA), the developed micropattern is clearly visible, as shown in Figure 7(c)–d, which is well matched with the designed pattern in Figure 7(c)–b. The size of the designed scaffold is around 6×6 cm, and was readily printed in 15 min. The process, from the design to the fabricated scaffold, is very similar with other rapid prototyping processes; this further supports the great application potential of PSTS for cell-aligned tissue engineering.

3.7 4D and beyond dynamic shape change

More interestingly, the PSTS printed thin film scaffold (thickness less than 300 μm) was autonomously bending or self-assembling into rolling structures when triggered by external stimulation (immersion in ethanol for 10 minutes) (Figure 7(d)). As shown in Figures 7(d) a–d, the blooming of flowers can be controlled with different sample thicknesses. We presume that the 4D mechanism is based on the generated internal strength during photolithography. Self-folding of hydrogels fabricated by UV exposure has been previously reported [31]. As UV light is attenuated through the thickness of the gel, a cross-link density gradient is formed. This gradient gives rise to differential swelling and a bending moment, resulting in the gel folding [31]. In this study, a cross-link density gradient may be generated during photolighography, which induces the internal strength. The release of the internal strength resulted in the self-folding of developed scaffolds, which makes our research fall into the realm of 4D printing as self-assembly right after 3D printing. The precise control of the bending of the fabricated scaffolds by adjusting thickness (Figure 7(d) e) provides a simple way to tailor the sample for catering various curvature of damaged tissues or organs, which is critical to achieve better tissue integration. Moreover, in our previous study, we investigated the shape memory property of the cured SOEA material which fixed a temporary shape at −18°C and fully recovered its original shape at human body temperature (37°C) [26]. The inherent capacity of shape memory polymers, to fix a temporary shape and recover their permanent structure under suitable stimuli, is similar in principle with the 4D dynamic process [32–35]. This specific capacity is also a widely used strategy to achieve minimally invasive surgeries. 4D printing shape memory materials is becoming a new, and rapidly expanding research area in the additive manufacturing field [26, 36–39]. Therefore, the scaffolds fabricated in our study not only perform self-folding right after printing (4D printing), but also possess shape memory properties (5D printing). The shape memory

process of a heart-shaped scaffold in the present study is demonstrated in Figure 8. These advanced properties provide great potential for both better integration of the scaffolds with damaged tissue or organ and minimally invasive surgery potential [4, 26].

3.8 Cardiomyogenic differentiation of hMSCs on the PSTS scaffolds

We investigated the cardiomyogenic differentiation of hMSCs on the 4D-fabricated scaffolds. The samples prepared by photolithography without aligned microstructures were used as control. Immunofluorescence analysis detected the expression of cardiac troponin I and sarcomeric-α-actinin (Figures 9(a), (b)). Greater marker expression on 4D scaffolds was observed, compared to control samples. Cell alignment was also observed on the 4D-printed scaffolds via α-actinin staining, further verifying our alignment hypothesis. Cardiomyogenic differentiation of hMSCs was also evaluated at the genetic level by determining the expression of MHC, desmin and MyoC using qRT-PCR. Expression of these markers was significantly up-regulated in hMSC groups cultured on 4D scaffolds, compared to the controls (Figure 9(c)). These results align with other reported work on the effect of forced alignment of neonatal rat mesenchymal stem cells undergoing cardiomyogenic differentiation on the time course and degree of functional integration with surrounding host cardiac tissue [12]. Thus, the aligned micro-surficial structures created with PSTS in the present study will significantly increase the application potential of the fabricated scaffold for cardiac patch applications.

4. Conclusions

The novel PSTS technique provides added value over current printing technologies. Photolithography is extremely fast, developing films in seconds with varied thicknesses [38]. More importantly, the photolithographic process induces a cross-link density gradient enabling scaffold self-bending, a 4D feature. Stereolithography is versatile for drawing complex surficial micropatterns, but is obviously slower than the photolithographic process for fabricating films because of its layer-by-layer process. The PSTS technique incorporates the advantages of photolithography and stereolithography for making self-assembling, patching scaffolds. In particular, the uneven-distribution of laser beam, subtly utilized in this study for generating microgroove structures for the first time, provides an inspiring way to develop topographical tissue engineering scaffolds.

4D scaffolds with unique surficial micropatterns are fabricated using the PSTS technique. The micropatterns are generated on a thin ink film residue (10μm depth), observed for the first time in our lab. The scaffolds exhibit excellent cell compatibility, and hMSCs actively grow along the developed micropatterns, resulting in uninterrupted cellular sheets. Compared to PDMS, the solidified SOEA exhibits significantly higher hMSC proliferation and does not differ statistically from PCL. Complex patterns are fabricated readily and rapidly. More interestingly, the scaffolds possess self-assembly and shape memory properties, which propel this research beyond the area of 4D printing. Cardiomyogenic differentiation of hMSCs on the printed scaffolds showed significantly increased marker expression, which implies its great potential for the cardiac tissue engineering applications.

Acknowledgments

The authors would like to thank the NSF MME program grant #1642186 for financial support.

References

1. Introduction. Am J Transplant. 2016; 16:8–10. [PubMed: 26755261]
2. Griffith LG, Naughton G. Tissue engineering - current challenges and expanding opportunities. Science. 2002; 295:1009–1014. [PubMed: 11834815]
3. Hollister SJ. Porous scaffold design for tissue engineering. Nat Mater. 2005; 4:518–524. [PubMed: 16003400]
4. Miao S, Zhu W, Castro NJ, Leng J, Zhang LG. Four-Dimensional Printing Hierarchy Scaffolds with Highly Biocompatible Smart Polymers for Tissue Engineering Applications. Tissue Eng Part C Methods. 2016; 22:952–963. [PubMed: 28195832]
5. Tibbits S. The emergence of "4D printing". TED Talk. 2013
6. Tibbits, S. 4D printing. SJET LLC; 2014. http://www.sjet.us/MIT_4D%20PRINTING.html
7. Tibbits S, McKnelly C, Olguin C, Dikovsky D, Hirsch S. 4D Printing and universal transformation. ACADIA. 2014:539–548.
8. Tibbits S. Design to Self-Assembly. Architect Design. 2012; 82:68–73.
9. Thomas, A., Campbell, ST., Garrett, Banning. The next wave: 4D printing programing the material world. The Atlantic Council of the United States; 2014.
10. Miao S, Castro N, Nowicki M, Xia L, Cui H, Zhou X, Zhu W, Lee S-j, Sarkar K, Vozzi G. 4D printing of polymeric materials for tissue and organ regeneration. Mater Today. 2017; 20:577–591.
11. Lanfer B, Seib FP, Freudenberg U, Stamov D, Bley T, Bornhäuser M, Werner C. The growth and differentiation of mesenchymal stem and progenitor cells cultured on aligned collagen matrices. Biomaterials. 2009; 30:5950–5958. [PubMed: 19674785]
12. Pijnappels DA, Schalij MJ, Ramkisoensing AA, van Tuyn J, de Vries AA, van der Laarse A, Ypey DL, Atsma DE. Forced alignment of mesenchymal stem cells undergoing cardiomyogenic differentiation affects functional integration with cardiomyocyte cultures. Circ Res. 2008; 103:167–176. [PubMed: 18556577]
13. Dang JM, Leong KW. Myogenic induction of aligned mesenchymal stem cell sheets by culture on thermally responsive electrospun nanofibers. Adv Mater. 2007; 19:2775–2779. [PubMed: 18584057]
14. Jahani H, Jalilian FA, Wu CY, Kaviani S, Soleimani M, Abassi N, Ou KL, Hosseinkhani H. Controlled surface morphology and hydrophilicity of polycaprolactone toward selective differentiation of mesenchymal stem cells to neural like cells. J Biomed Mater Res Part A. 2015; 103:1875–1881.
15. Yang F, Murugan R, Wang S, Ramakrishna S. Electrospinning of nano/micro scale poly (L-lactic acid) aligned fibers and their potential in neural tissue engineering. Biomaterials. 2005; 26:2603–2610. [PubMed: 15585263]
16. Lim SH, Liu XY, Song H, Yarema KJ, Mao H-Q. The effect of nanofiber-guided cell alignment on the preferential differentiation of neural stem cells. Biomaterials. 2010; 31:9031–9039. [PubMed: 20797783]
17. Kim J, Staunton JR, Tanner K. Independent control of topography for 3D patterning of the ECM microenvironment. Adv Mater. 2016; 28:132–137. [PubMed: 26551393]
18. Wang ZY, Teoh SH, Johana NB, Chong MSK, Teo EY, Hong M-h, Chan JKY, San Thian E. Enhancing mesenchymal stem cell response using uniaxially stretched poly (ε-caprolactone) film micropatterns for vascular tissue engineering application. J Mater Chem B. 2014; 2:5898–5909.
19. Wang ZY, Lim J, Ho YS, Zhang QY, Chong MS, Tang M, Hong MH, Chan JK, Teoh SH, Thian ES. Biomimetic three-dimensional anisotropic geometries by uniaxial stretching of poly (ε-caprolactone) films: Degradation and mesenchymal stem cell responses. J Biomed Mater Res Part A. 2014; 102:2197–2207.

20. Wang ZY, Teo EY, Chong MSK, Zhang QY, Lim J, Zhang ZY, Hong MH, Thian ES, Chan JKY, Teoh SH. Biomimetic three-dimensional anisotropic geometries by uniaxial stretch of poly (ε-caprolactone) films for mesenchymal stem cell proliferation, alignment, and myogenic differentiation. Tissue Eng Part C Methods. 2013; 19:538–549. [PubMed: 23198964]
21. Béduer A, Vieu C, Arnauduc F, Sol J-C, Loubinoux I, Vaysse L. Engineering of adult human neural stem cells differentiation through surface micropatterning. Biomaterials. 2012; 33:504–514. [PubMed: 22014459]
22. Hsu, Sh, Su, CH., Chiu, IM. A novel approach to align adult neural stem cells on micropatterned conduits for peripheral nerve regeneration: a feasibility study. Artif Organs. 2009; 33:26–35. [PubMed: 19178438]
23. Barry RA, Shepherd RF, Hanson JN, Nuzzo RG, Wiltzius P, Lewis JA. Direct -Write Assembly of 3D Hydrogel Scaffolds for Guided Cell Growth. Adv Mater. 2009; 21:2407–2410.
24. Lind JU, Busbee TA, Valentine AD, Pasqualini FS, Yuan H, Yadid M, Park S-J, Kotikian A, Nesmith AP, Campbell PH. Instrumented cardiac microphysiological devices via multimaterial three-dimensional printing. Nat Mater. 2017; 16:303–308. [PubMed: 27775708]
25. Miao S, Wang P, Su Z, Zhang S. Vegetable-oil-based polymers as future polymeric biomaterials. Acta Biomater. 2014; 10:1692–1704. [PubMed: 24012607]
26. Miao S, Zhu W, Castro NJ, Nowicki M, Zhou X, Cui H, Fisher JP, Zhang LG. 4D printing smart biomedical scaffolds with novel soybean oil epoxidized acrylate. Sci Rep. 2016; 6:27226. [PubMed: 27251982]
27. Hosseini Y, Zellner P, Agah M. A single-mask process for 3-D microstructure fabrication in PDMS. J Microelectromech Syst. 2013; 22:356–362.
28. Castro NJ, O'Brien J, Zhang LG. Integrating biologically inspired nanomaterials and table-top stereolithography for 3D printed biomimetic osteochondral scaffolds. Nanoscale. 2015; 7:14010–14022. [PubMed: 26234364]
29. Cui H, Nowicki M, Fisher JP, Zhang LG. 3D Bioprinting for Organ Regeneration. Adv Healthc Mater. 2016; 6:1601118.
30. Yim EK, Darling EM, Kulangara K, Guilak F, Leong KW. Nanotopography-induced changes in focal adhesions, cytoskeletal organization, and mechanical properties of human mesenchymal stem cells. Biomaterials. 2010; 31:1299–1306. [PubMed: 19879643]
31. Kaäpylä E, Delgado SM, Kasko AM. Shape-Changing Photodegradable Hydrogels for Dynamic 3D Cell Culture. ACS Appl Mater Interfaces. 2016; 8:17885–17893. [PubMed: 27322508]
32. Zhao Q, Qi HJ, Xie T. Recent progress in shape memory polymer: New behavior, enabling materials, and mechanistic understanding. Prog Polym Sci. 2015; 49:79–120.
33. Hager MD, Bode S, Weber C, Schubert US. Shape memory polymers: Past, present and future developments. Prog Polym Sci. 2015; 49:3–33.
34. Miao S, Callow N, Wang P, Liu Y, Su Z, Zhang S. Soybean oil-based polyurethane networks: shape-memory effects and surface morphologies. J Am Oil Chem Soc. 2013; 90:1415–1421.
35. Miao S, Wang P, Su Z, Liu Y, Zhang S. Soybean oil-based shape-memory polyurethanes: Synthesis and characterization. Eur J Lipid Sci Technol. 2012; 114:1345–1351.
36. Zhou Y, Huang WM, Kang SF, Wu XL, Lu HB, Fu J, Cui H. From 3D to 4D printing: approaches and typical applications. J Mech Sci Technol. 2015; 29:4281–4288.
37. Pei E. 4D Printing: dawn of an emerging technology cycle. Assembly Autom. 2014; 34:310–314.
38. Huang L, Jiang R, Wu J, Song J, Bai H, Li B, Zhao Q, Xie T. Ultrafast Digital Printing toward 4D Shape Changing Materials. Adv Mater. 2016; 29:1605390.
39. Zarek M, Layani M, Eliazar S, Mansour N, Cooperstein I, Shukrun E, Szlar A, Cohn D, Magdassi S. 4D printing shape memory polymers for dynamic jewellery and fashionwear. Virtual Phys Prototyp. 2016; 11:263–270.

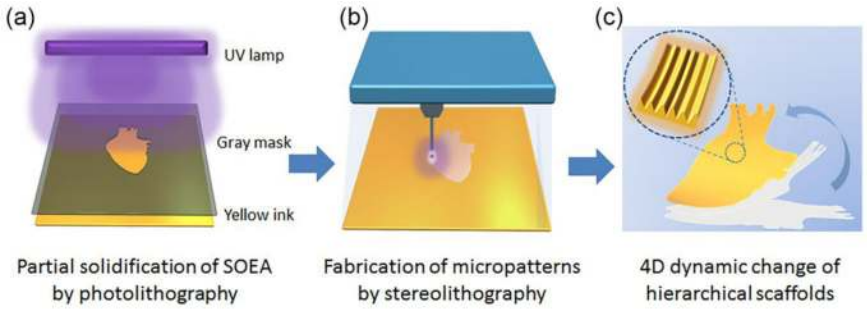

Figure 1.

Schematic illustration of the photolithographic-stereolithographic-tandem process. (a) The yellow ink is covered with a gray mask. The exposed ink (the heart shape in the center of the image) will be partially solidified under UV lamp. An unsolidified ink film (around 10 μm thick) will remain on its surface. (b) The unsolidified ink film can be further solidified using a laser source. Micropatterns are drawn using a laser head on the unsolidified ink film forminghierarchical structures. (c) Under external stimulus, the flat scaffold can bend to perform a 4D effect.

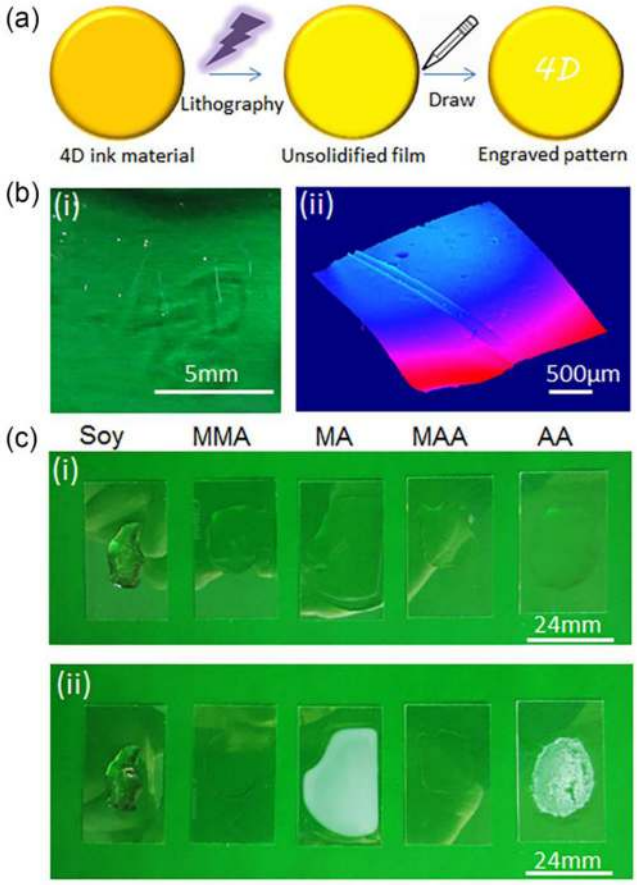

Figure 2.

Observation of the unsolidified thin ink film after photolithography. (a) Operation procedure. (b) Inspection of the drawn patterns on the unsolidified thin ink film: (i) Photo of the pattern. (ii) Microscopy of the pattern after surface plot treatment. (c) Photolithographic polymerization of different monomers: (i) Before polymerization. (ii) After photolithography. Soy, polymerized SOEA; MMA, methyl methacrylate acid; MA, methacrylate acid; MAA, methyl acrylate acid, and AA, acrylate acid.

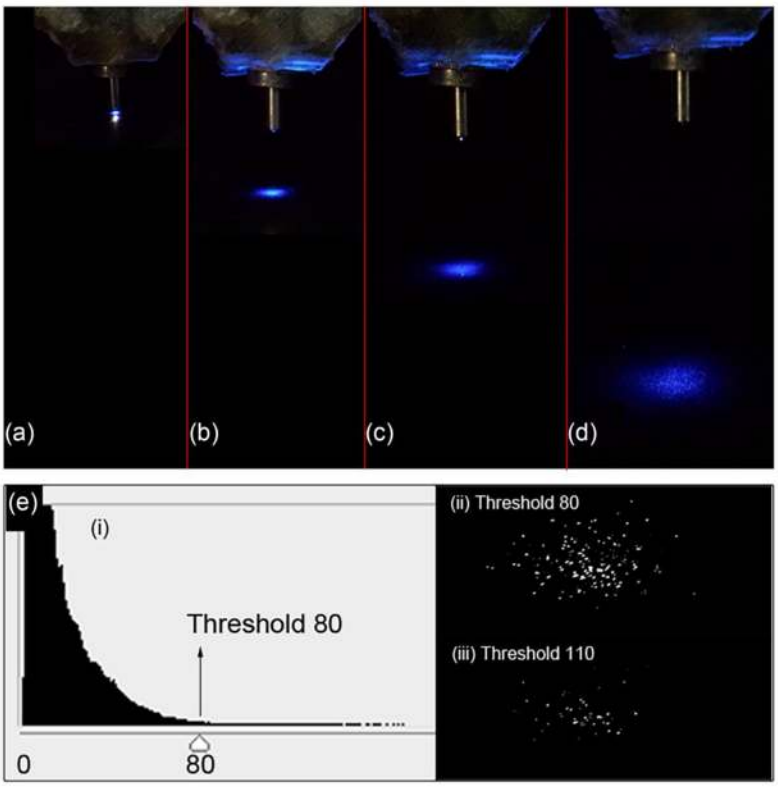

Figure 3.

The laser beam of stereolithography. (a) The distance between the laser and the dark board is 2 mm which is used for printing scaffolds. (b) The distance is 1 cm. (c) The distance is 2 cm. (d) The distance is 4 cm. (e) Analysis of the laser dot on dark board shown in (d). (i) Threshold chart. (ii) The light distribution as threshold value is 80. (iii) The distribution of laser light as threshold value is 110.

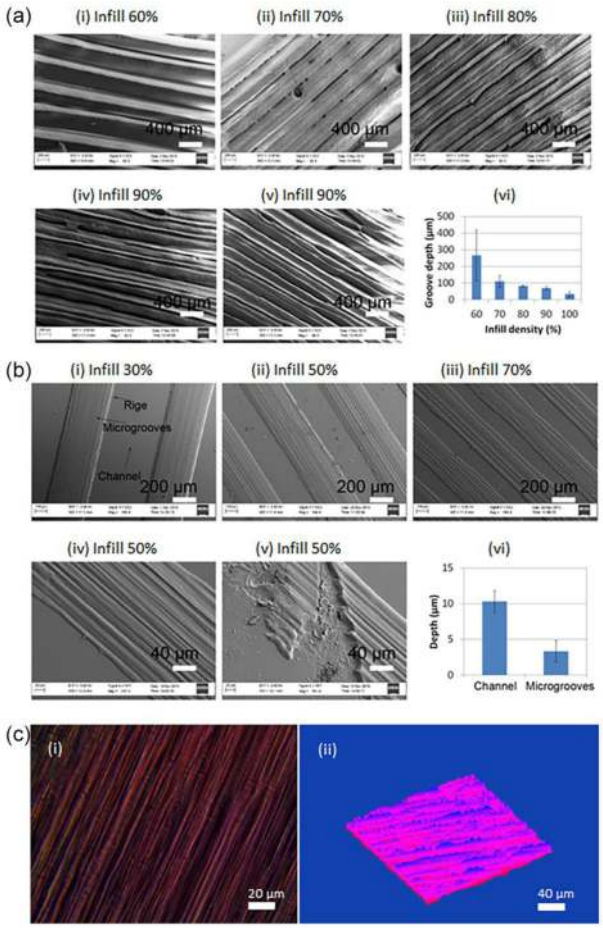

Figure 4.

SEM and microscope images of the fabricated samples. (a) (i–v) SEM images of stereolithographic samples with different infill densities and (vi) the groove depth chart. (b) (i–iii) SEM images of the samples developed by PSTS with different infill densities. (iv) The microgrooves on the ridge. (v) The fractured profile of the ridge and (vi) the depth chart. (c) (i) Microscope images of the microgrooves on the ridge. (ii) The microscope image after surface plot treatment.

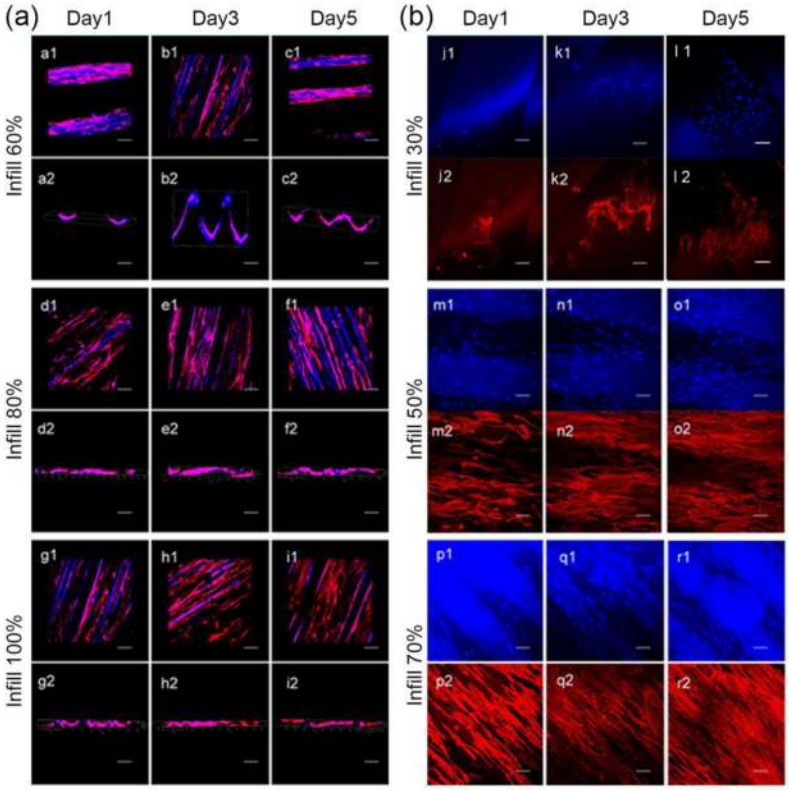

Figure 5.

Confocal images of hMSC spreading on different micropatterns. The hMSCs were dyed with Texas Red (red) and 4′,6-diamidino-2-phenylindole (blue). (A) (a1–i1) Top view of stereolithographic samples. (a2–i2) Side view of stereolithographic samples; (B) (j1–r1) The separated view of blue dye for the PSTS samples. (j2–r2) The separated view of red dye for the PSTS samples. Scale bars, 100 μm.

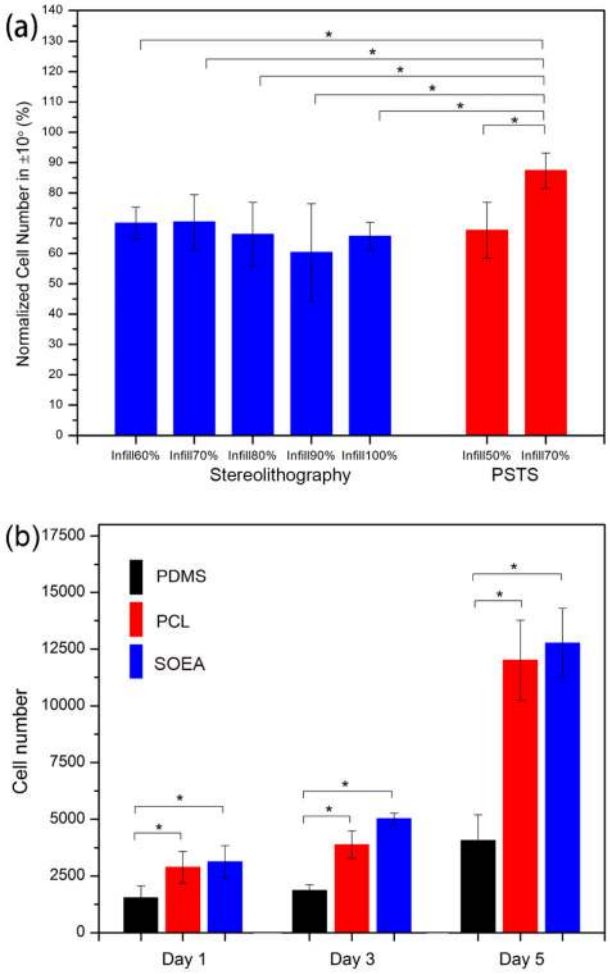

Figure 6.

(a) Alignment quantification of hMSCs cultured on different micropatterns. Data represent the mean ± standard deviation, n=6. *p<0.05. (b) Proliferation of hMSCs on PDMS, PCL and polymerized SOEA, respectively. Data represent the mean ± standard deviation, n=6. *p<0.05.

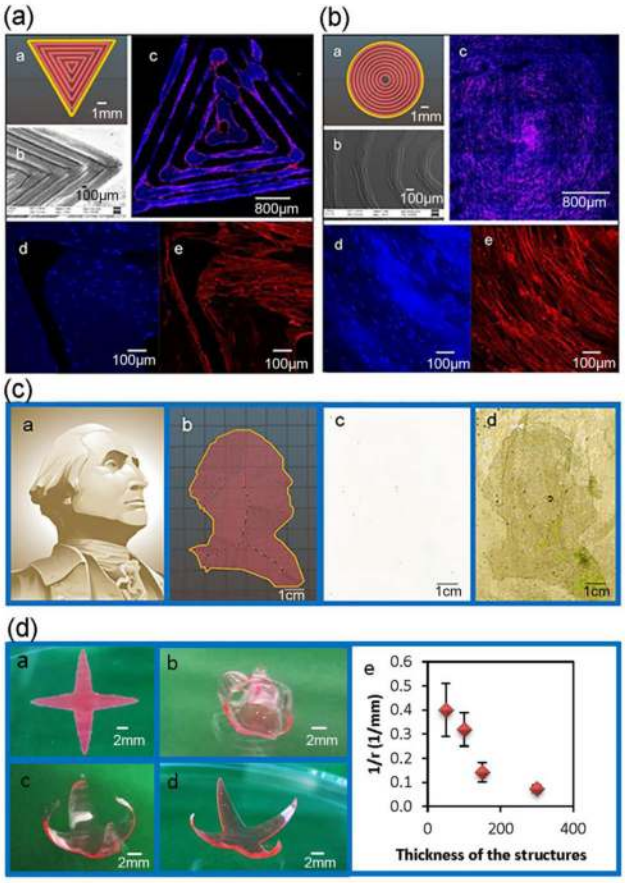

Figure 7.

(a) A triangle micropattern by stereolithography with an infill density of 70%. a, The designed triangle pattern in Slic3r; b, The SEM image of the printed triangle scaffold; c, The confocal micrograph of hMSC growth on the microstructure (both blue and red dye); d, The separated view of blue dye corresponding to cell's nuclei; e, The separated view of red dye corresponding to cells' cytoskeleton. (b) A circular micropattern developed by PSTS with an infill density of 70%. a, The designed circular pattern in Slic3r; b, The SEM image of the printed circular scaffold; c, The confocal micrograph of hMSC growth on the microstructure (both blue and red dye); d, The separated view of blue dye corresponding to cell's nuclei; e, The separated view of red dye corresponding to cells' cytoskeleton. (c) The demonstration of this technique for complex and large patterns in an efficient way. a, The logo of The George Washington University; b, The designed pattern in Slic3r; c, The scanned image of the printed scaffold, approximately 6×6 cm; d, The scanned image after increasing brightness and contrast in a Photoshop software. (d) The dynamic 4D shape change controlled by different thicknesses. a, 4D star structure after printing. b–d, the shape change after external stimulation (b, 100 μm thick; c, 150 μm thick; and d, 300 μm thick). Samples were stained with Nile red (0.01% in the ink). e, The thickness vs. curvature.

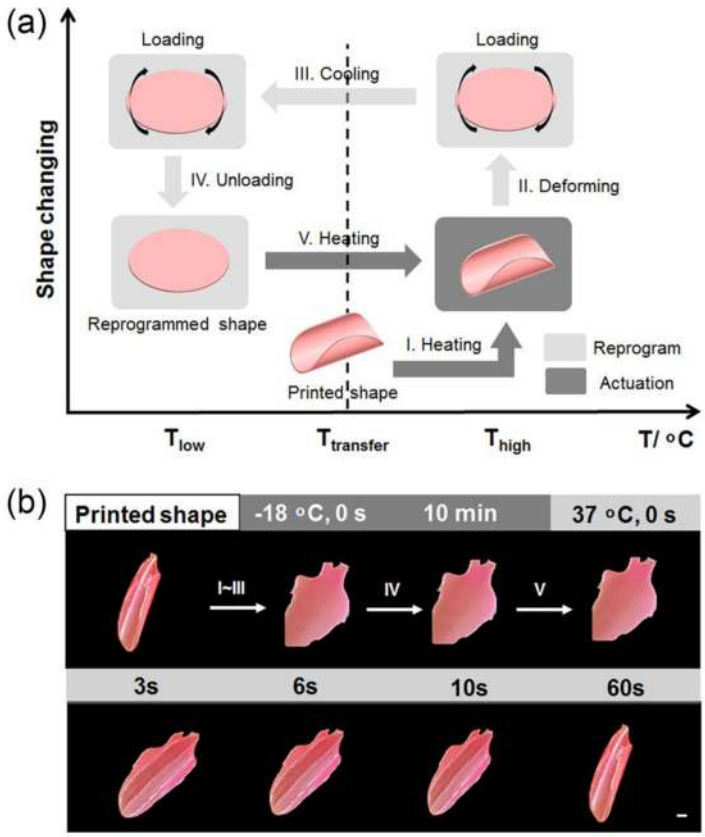

Figure 8.

Beyond 4D printing – shape memory effect. (A) Illustration of the shape memory process. I, to increase temperature over transferring temperature; II, to exert a shape change with enforced restriction; III, fix a temporary shape at lower temperature; IV to remove external enforced restriction; and V, to increase temperature to recover the original shape. (B) Demonstration of the shape memory process with 4D printed heart-shaped construct. The flat heart-shape construct gradually recovered its original rolling shape as the construct was put in a 37 °C environment. Scale bar, 2 mm.

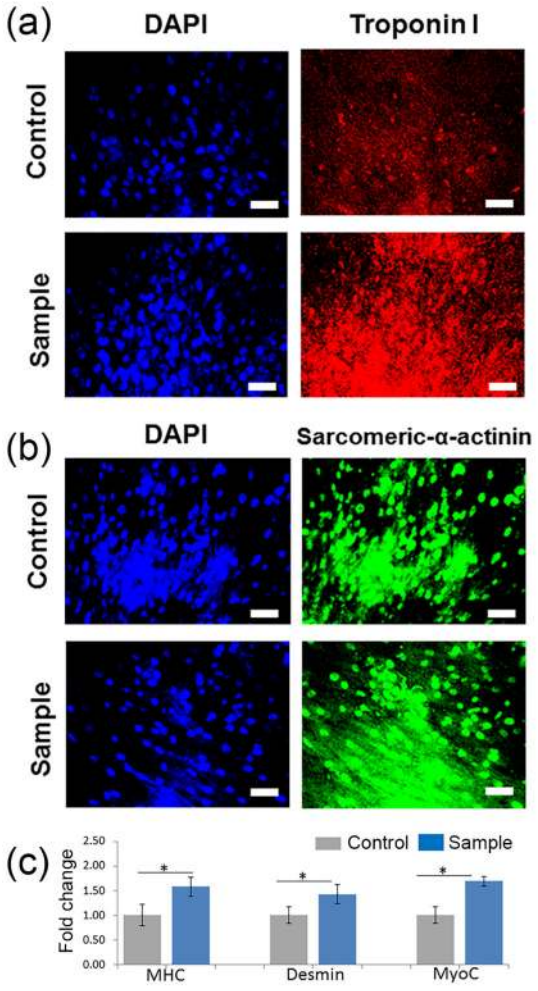

Figure 9.

Cardiomyogenic differentiation of hMSCs on the 4D fabricated scaffolds and the controls. (a) The expression of cardiac troponin I. (b) The expression of sarcomeric-α-actinin. (c) The expression of MHC, desmin and MyoC determined using qRT-PCR.